On the Value of LES Models for Evaluating Spatio-Temporal Tropospheric Variability in Multitemporal SAR Interferograms

Fengming Hu, *Member, IEEE*, Kevin C. Helfer, A. Pier Siebesma, and Ramon F. Hanssen, *Senior Member, IEEE*

***Abstract*—Atmospheric delay has a profound impact on synthetic aperture radar (SAR) interferometry, inducing a spatial signal that significantly devaluates interferometric products. While the wide-scale variability of the atmosphere can be adequately modeled with global or regional weather models, it is especially the turbulent and convective part of the atmosphere at smaller spatial and temporal scales that is typically poorly captured. Due to the high resolution and precision of InSAR, there is a need for a realistic modeling of the 3-D distribution of turbulent refractivity in the boundary layer. This would enable assessment of the impact of a temporal or spatial model misalignment on the interferometric products, and contribute to studying the impact for future SAR missions. Here we test the feasibility of an advanced large Eddy simulation (LES) model to simulate a time-series refractivity distribution with a high spatio-temporal resolution to show the spatio-temporal variability of the troposphere on short time scales. We found for a fair-weather situation that the LES model produces realistic atmospheric simulations that match stochastically with results found in interferometric studies and that tropospheric delay variation leads to significant phase gradients within several minutes. This implies that even when using an (unrealistic) perfect weather model with resolutions similar to the SAR image, realizations that are several minutes apart from the time of the SAR acquisition will lead to significant phase errors. We propose the use of LES models as a realistic instrument to perform InSAR quality-assessments and for the development and simulation for future missions.**

***Index Terms*—Large-eddy simulation (LES), multitemporal interferometric synthetic aperture radar (InSAR), tropospheric delay.**

I. Introduction

SYNTHETIC aperture radar (SAR) plays an important role in remote sensing, by observing the Earth's surface with a large coverage and acquiring information about its physical properties. Using interferometric (In)SAR, the interferometric phase denotes the path delay between two SAR observations along the line of sight, reflecting the topographic height difference, surface motion, and atmospheric delay [1], [2], [3], [4], [5]. Depending on the purpose of the interferometric study, the atmospheric delay is either a nuisance signal that needs to be mitigated, or the meteorological signal of interest that reveals information on the integrated refractivity and water vapor distribution [6], [7]. For both objectives, atmospheric dynamics at meso-gamma-scales (2–20 km) are most challenging, as the synoptic, meso-alpha, and meso-beta scales are better recoverable with global and regional numerical weather prediction (NWP) models [8], [9].

As a nuisance signal, we need to better understand the nature of the variability of the atmospheric delay signal at meso-gamma scales. For these scales, temporal and spatial resolvability are intimately entwined, which implies that a misalignment, either temporal or spatial, has a significant impact. Thus, there is a limit to the use of weather models for atmospheric correction of SAR interferograms, below which a correction is likely to result in an adverse negative effect.

As a meteorological signal of interest, the precision and spatial resolution of InSAR holds significant potential for assimilation into NWP models, e.g., for identifying extreme rain fall [10], [11]. Moreover, future geosynchronous (GEO) SAR missions potentially have a short revisit time and large coverage of potentially more than 1000 km [12], leading to an opportunity to obtain real-time surface observation for fast disaster warning [13]. Such short temporal baselines enable the frequent and continuous production of integrated refractivity maps with high resolution. Near real-time integrated refractivity can improve weather forecasting and consequently provide early warnings for severe weather or increased risks for landslides [14].

Large eddy simulation (LES) models use computational fluid dynamics to model turbulence. Simulations of moist convection are run at resolutions high enough to resolve convection explicitly [8], making them very well suited for studying meso-gamma scale atmospheric signal in InSAR. Yet, the use of LES models for InSAR has not been investigated in depth thus far. To investigate the value of LES models for this purpose, we conduct a proof-of-concept study of a simulated fair-weather day that depicts typical weather conditions over mid-latitude land. We introduce a standard approach to generate atmospheric interferograms, i.e., synthetic interferograms only sensitive to

Manuscript received 17 March 2022; revised 26 June 2022; accepted 9 August 2022. Date of publication 22 August 2022; date of current version 2 September 2022. This work was supported by the Hydroterra Phase-0 Science and Requirement project by ESA. *(Correponding author: Fengming Hu.)*

Fengming Hu is with the Key Laboratory for Information Science of Electromagnetic Waves (MoE), Fudan University, Shanghai 200433, China, and also with the Department of Geoscience and Remote Sensing, Delft University of Technology, 2628 Delft, The Netherlands (e-mail: fm_hu@fudan.edu.cn).

Kevin C. Helfer is with the Department of Geoscience and Remote Sensing, Delft University of Technology, 2628 Delft, The Netherlands. He is now with Infoplaza B.V., Sleepboot 5, 3991 CN Houten, The Netherlands (e-mail: k.c.helfer@tudelft.nl).

A. Pier Siebesma and Ramon F. Hanssen are with the Department of Geoscience and Remote Sensing, Delft University of Technology, 2628 Delft, The Netherlands (e-mail: a.p.siebesma@tudelft.nl; R.F.Hanssen@tudelft.nl).

Digital Object Identifier 10.1109/JSTARS.2022.3200554

This work is licensed under a Creative Commons Attribution 4.0 License. For more information, see https://creativecommons.org/licenses/by/4.0/

atmospheric delay variability, constructed from a hypothetical ideal SAR mission, showing the time-varying characteristics of the troposphere. We refer to them as "synthetic interferograms" in this study. First, the Dutch atmospheric large eddy simulation (DALES) model and its output atmospheric parameters are briefly reviewed, including details of the transformation from model parameters to refractivity. Slant delays are calculated with variable orbit parameters. Finally, time series of atmospheric interferograms are generatedand the impacts of their spatio-temporal characteristics are shown.

II. Interferometric Delay

In this part, we introduce the standard approach to generate the synthetic interferograms using the atmospheric parameters simulated by the DALES model. It contains four parts, i.e., parameters conversion, refractivity calculation, ray tracing the slant radar path, and interferogram generation.

A. Definition of the Slant Delay

The two-way slant delay difference $2\delta_p$ for a location p at acquisition t_1 expressed as phase delay (ψ_p) is given by

$$\psi_{p,t_1} = \frac{4\pi}{\lambda}\delta_{p,t_1} \tag{1}$$

where λ is the radar wavelength. The observed phase difference ϕ_p in the interferogram between acquisitions t_1 and t_2 is

$$\phi_p = \frac{4\pi}{\lambda}(\delta_{p,t_2} - \delta_{p,t_1}). \tag{2}$$

Given the antenna position a, the delay at the image pixel p is obtained by integrating along the path l of the line of sight using the refractivity N, which is defined as [2], [15]

$$\delta_{p,t} = 10^{-6}\int_{l=p}^{a} N\big(x(l), y(l), z(l), t\big)dl. \tag{3}$$

Considering all types of atmospheric delay, the original expressions of the refractivity can be written as [16]

$$N = k_1\frac{P_d}{T} + \left(k_2\frac{e}{T} + k_3\frac{e}{T^2}\right) + k_4\frac{n_e}{f^2} + k_5\, W \tag{4}$$

where P_d is partial pressure of dry air, e denotes partial pressure of water vapor, T is temperature, n_e is the electron density per cubic meter, f is the radar frequency, and W is the liquid water content. The constants used in this article are $k_1 = 77.6$ K hPa^{-1}, $k_2 = 70.4$ K hPa^{-1}, $k_3 = 3.739 \times 10^5$ K^2 hPa^{-1}, $k_4 = 4.028 \times 10^7$ m^{-3}, and $k_5 = 1.45$ m^{3}g^{-1}. The last two terms in (4) are the ionospheric term and the liquid term, which are not considered in this study. The other three terms are referred to as the tropospheric terms.

Assuming that the total atmospheric pressure is $P = P_d + e$, the tropospheric refractivity N_{tro} is the summation of a hydrostatic and a "wet" component

$$N_{\text{tro}} = k_1\frac{P}{T} + \left(k_2'\frac{e}{T} + k_3\frac{e}{T^2}\right) \tag{5}$$

where $k_2' = k_2 - k_1 R_d R_v^{-1}$, with $R_d = 287.053$ J K^{-1} kg^{-1} and $R_v = 461.524$ J K^{-1} kg^{-1}.

B. Parameters in the DALES Model

The numerical atmospheric model used in this research is DALES, the Dutch Atmospheric Large Eddy Simulation model [17], which can provide reliable results for a multitude of atmospheric conditions. The LES uses liquid water potential temperature θ_L and specific humidity q_v as prognostic variables and a diagnostic hydrostatic total pressure p and liquid water specific humidity q_l. Since the tropospheric refractivity depends on partial pressure of water vapor, total pressure and temperature, see (5), we need to convert the DALES parameters for e and T. The definition of the specific humidity is

$$q_v = \frac{m_v}{m_t} \tag{6}$$

where m_v denotes the specific mass of water vapour and $m_t = m_d + m_v$ denotes the sum of the dry air specific mass and the specific mass of water vapour. Using the gas law and Dalton's law we can rewrite q_v in terms of the vapor pressure as [17]

$$q_v = \epsilon\frac{e}{p + e(\epsilon - 1)} \tag{7}$$

where $\epsilon = R_d/R_v$. Assuming that q_v is much smaller than 1, inverting this gives the desired relation

$$e = \frac{p}{\epsilon}\frac{q_v}{1 + (1/\epsilon - 1)q_v} \simeq \frac{p}{\epsilon}q_v. \tag{8}$$

To compute the temperature T, we use the linearized form of the liquid water potential temperature θ_L in DALES [15], [18]

$$\theta_L \equiv \frac{1}{\Pi}T - \frac{L_v}{c_p\Pi}q_l \tag{9}$$

where the latent heat of vaporization $L_v = 2.25 \times 10^6$ J $\cdot$ kg^{-1}, and the specific heat of dry air $c_p = 1004$ J $\cdot$ K$^{-1}\cdot$kg^{-1}. We use the Exner function defined as $\Pi \equiv (\frac{p}{p_0})^{R_d/c_p}$ and the standard pressure $p_0 = 1000$ hPa. Inverting this allows to write the temperature in terms of θ_l, q_l, and pressure p

$$T = \Pi\,\theta_L + \frac{L_v}{c_p}q_l. \tag{10}$$

Finally, with (8) and (10), the 4-D refractivity distribution can be obtained using (5) with all derived parameters.

We compute the tropospheric delay along the line of sightusing ray-tracing [19] based on the SAR geometry. In Fig. 1, the radar signal passes the troposphere from point B to illuminate target A. Although the path of the signal is not a straight line, the contribution of the refractivity change due to the bending error is negligible for typical SAR incidence angles [2], [20]. Thus, the total tropospheric delay for one acquisition is obtained by integrating the refractivity from the elevation of the target A to the total height of the troposphere, cf. (3). Subsequently, the tropospheric delay is calculated using (1).

C. Interferogram Generation

Considering m SAR acquisitions, $m-1$ independent interferograms are generated and the combination of the interferograms can be one of the following two types. In the *single master* approach, only one SAR image is chosen as the master image,

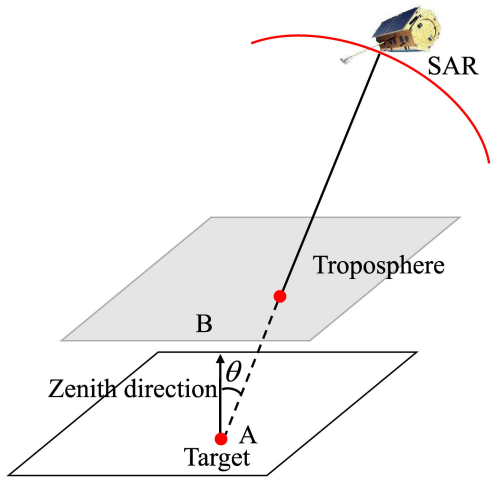

Fig. 1. Simplified sketch of radar signal propagation in the troposphere.

and all interferograms are obtained by

$$\phi_p^i = \text{wrap}\left\{\psi_p^{i+1} - \psi_p^1\right\} \tag{11}$$

where wrap$\{\dots\}$ denotes the wrapping operator [2]. In the *daisy chain* approach, all interferograms are generated using two subsequent SAR acquisitions, as given by

$$\phi_p^i = \text{wrap}\left\{\psi_p^{i+1} - \psi_p^i\right\}. \tag{12}$$

Time series interferograms only show the relative changes of the interferometric phase over time. Retrieving the undifferenced integrated refractivity distribution corresponding to each SAR acquisition can be accomplished by adding a constraint using external data [21], such as MODIS [22] and GNSS data [7] to fix the observation in one of the epoch.

III. Simulation

We conduct large-eddy simulations using DALES, version 4.2. The simulation setup is based on radiosonde and ground observations on 21 June 1997 at the Southern Great Plains site, an extensive atmospheric measurement site in Oklahoma and Kansas, USA [23]. The simulation covers an area of 49.3 $\times$ 49.3 km^2 and is characterized by shallow cumulus convection with a cloud cover between 20% and 30%. Shallow cumulus clouds are typical fair-weather clouds and a common cloud type over continental mid-latitudes [24]. They can be simulated very well in LES [23] and are thus ideally suited for the present proof-of-concept study. After 6 h of simulation time (when sufficient atmospheric turbulence and clouds have developed), we produce 3-D output at a temporal resolution of 10 s for 15 min of simulation time to yield the 4-D refractivity distribution.The relevant parameters are shown in Table I.

The most spatio-temporally variable parameters in the simulated refractivity distribution are the specific humidity q_v and the liquid water potential temperature θ_L. Fig. 2 shows the vertical profile of these parameters, averaged over the entire spatial domain per elevation level. The average of the specific humidity, see Fig. 2(a), decreases significantly at higher altitudes,especially in the range from 1000 to 2500 m. This implies

TABLE I
Parameters of the First Time-Series Refractivity Distribution in the DALES Simulation

Parameters	values
temporal resolution (s)	10
simulation temporal extent (min)	15
scale (km $\times$ km)	49.3$\times$ 49.3
horizontal resolution (m$\times$m)	40$\times$ 40
maximal height (m)	4500
vertical resolution (m)	40

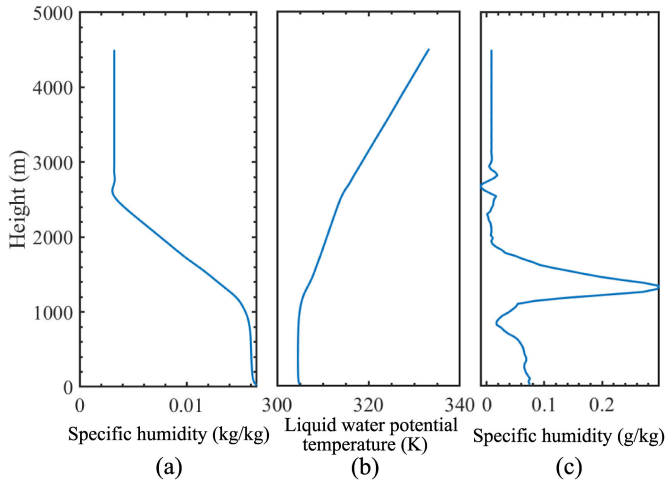

Fig. 2. Vertical distribution of (a) specific humidity, and (b) liquid water potential temperature, averaged over the entire domain at t_0. (c) Difference of the specific humidity between t_0, the first epoch, and $t_0 + 15$ min (the last epoch) as a function of height.

that most of the wet delay occurs lower than 2500 m. The liquid water potential temperature, see Fig. 2(b), stays nearly constant until 1000 m and increases significantly above 1000 m. Finally, the difference in the specific humidity between the first (t_0) and the last epoch ($t_0 + 15$ min) as a function of height is shown in Fig. 2(c), indicating that the water vapor is increasing during the simulated period. Although the difference of the specific humidity within 15 min is small ($\sim$0.3 g/kg), it will lead to a significant change in partial pressure of water vapor, see (8). Additionally, the maximum value of the difference is situated at a height of 1340 m, which demonstrates that the total water vapor varies most significantly between 1000 and 2000 m, which is the height where clouds are present.

In (3) and (5), the tropospheric delay is divided into two parts, the hydrostatic and the wet delay. Fig. 3 shows the vertical delay for both components at t_0 for a subset of 6.7 $\times$ 6.7 km of the original dataset. While the absolute value of the hydrostatic delay is[1] $\sim$914 mm, which is larger than that of the wet delay, $\sim$218 mm, the spatial variability range of the wet delay is dominant over that of both temperature and pressure: the spatial range of the hydrostatic delay ($\sim$1 mm), is much smaller than that of wet delay ($\sim$16 mm), see Fig. 3(a) and (b).

[1]Note that the DALES model is evaluated up to a maximum elevation of 4.5 km. As a consequence the total hydrostatic delay is less than typically experienced when dealing with the actual atmosphere in space geodetic methods.

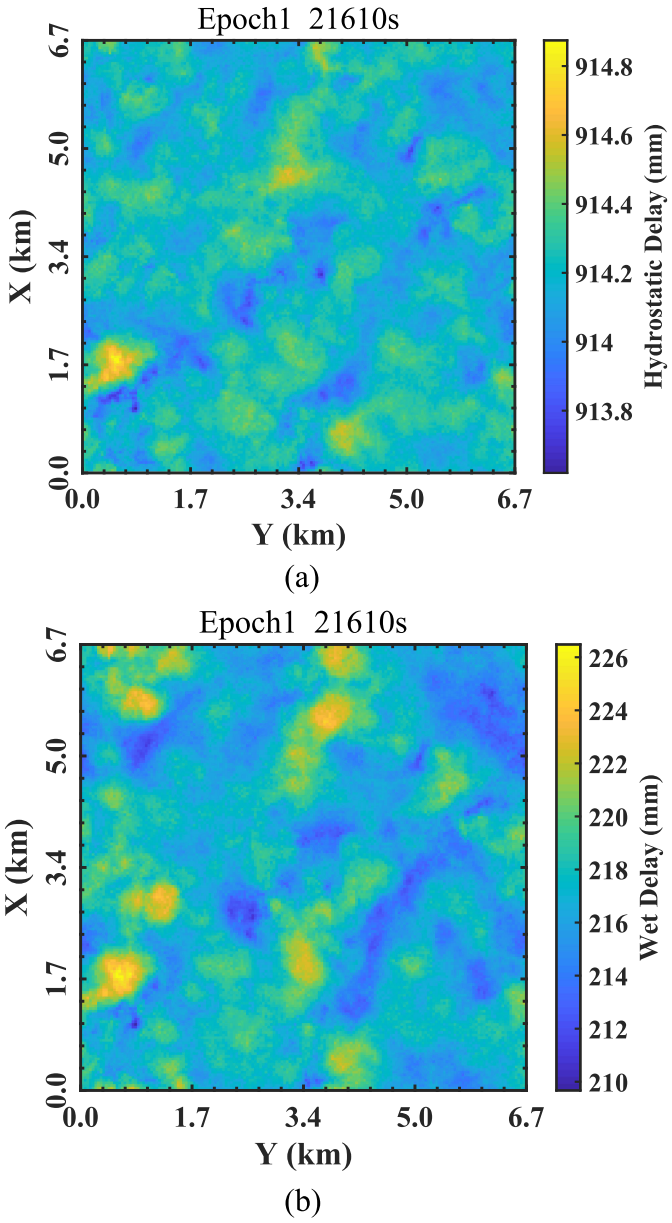

Fig. 3. Vertical tropospheric delay at t_0 for epoch 1. (a) Hydrostatic delay. (b) Wet delay. Note the difference in the colorbar values and ranges.

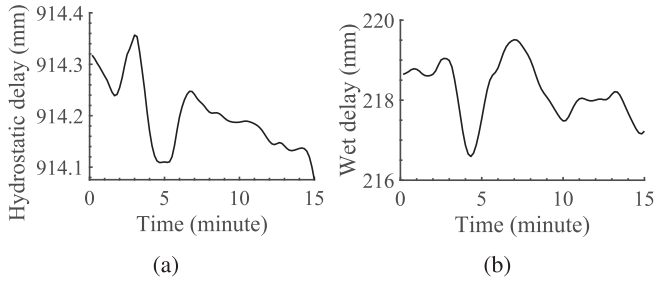

Fig. 4. Tropospheric delay time series for one location. (a) Hydrostatic delay. (b) Wet delay.

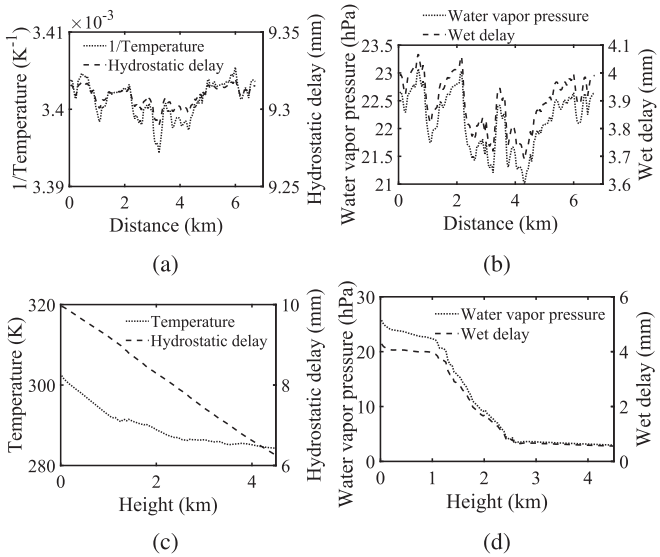

Fig. 5. Comparison of spatial changes between atmospheric parameters and tropospheric delay. (a) and (b) are horizontal variations at a height of 900 m, and (c) and (d) are vertical variations. (a) and (c) are spatial variations of hydrostatic delay and temperature, (b) and (d) are spatial variations of water vapor pressure and wet delay.

The tropospheric delay time series of the hydrostatic and the wet delay, evaluated at one position, is shown in Fig. 4(a) and (b), respectively. This confirms that also the temporal variation of the hydrostatic delay is smaller than that of wet delay. The hydrostatic delay varies over ~ 0.4 mm, while the wet delay varies over ~ 4 mm during the 15' of the evaluation. Thus, the effects of the hydrostatic delay between subsequent acquisitions are extremely small (i.e., negligible over the synthetic aperture integration of a GEO InSAR mission). To investigate the sensitivity of the observed signal delays to the atmospheric parameters, we compared T^{-1} and e, cf. (5), with the delay, for a horizontal cross section of the delay at t_0. Fig. 5(a) and (b) show the horizontal variation of tropospheric delay, here evaluated at a height of 900 m, which means that the tropospheric delay is integrated until 900 m and the parameters including temperature and water vapor are computed at 900 m. It shows that the spatial variation of the hydrostatic delay is highly correlated with the inverse temperature (0.9996) while that of the wet delay is very correlated with water vapor pressure (0.9998). Additionally, Fig. 5(c) and (d) show that the vertical range of variability of the tropospheric delay is much more than the horizontal variability. The vertical variability of hydrostatic delay is less correlated with the temperature while the vertical variability of the wet delay shows a strong correlation with water vapor pressure.

IV. Analysis of Synthetic Interferograms

A. Statistical Characteristics

Using a C-band radar wavelength of 0.056 m, two "tropospheric" synthetic interferograms aresimulated, assuming vertical (zenith) delays, i.e., not projected to the line of sight. Based on the assumption that the refractivity distribution can be considered frozen within a 10-s window, a 15-min (15') synthetic interferogram (combining epoch 1 and epoch 90) with a color

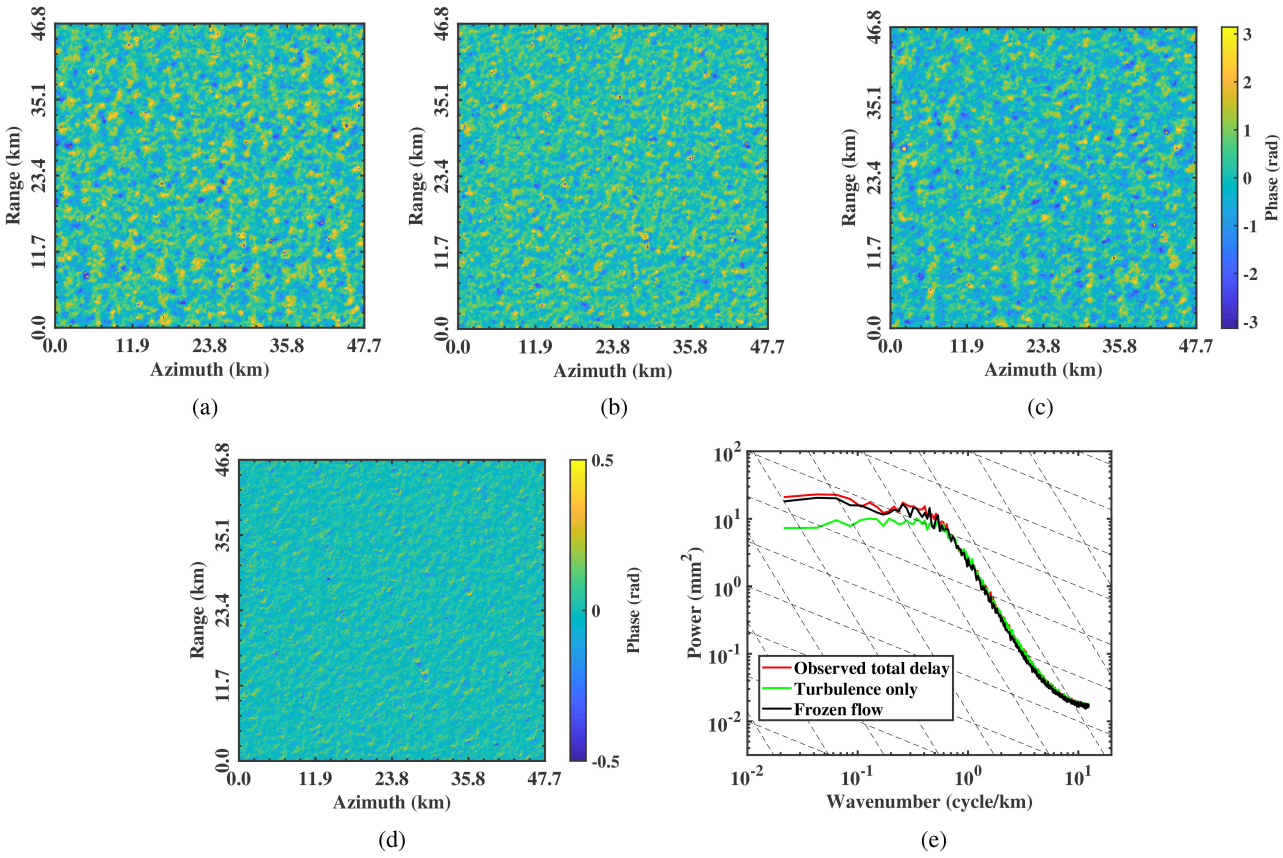

Fig. 6. Tropospheric synthetic interferogram over (a) 15 min (epoch 1–90) and (d) 10 s (epoch 89–90). Note the difference in the colorbar range. (b) and (c) are turbulence-only and frozen flow synthetic interferograms of 15 min synthetic interferograms, respectively. (e) shows the corresponding power spectra of (a), (b), and (c). (a) Tropospheric delay. (b) Turbulence. (c) Frozen flow. (d) Daisy chain. (e) Power spectra.

bar range of 2π rad, and a 10-s (10") synthetic interferogram (combining epochs 89 and 90) with a color bar range of 1 rad are shown in Fig. 6(a) and (d), respectively, demonstrating the significant influence of a longer temporal separation.

The short-term tropospheric synthetic interferogram signal can now be disentangled into two temporal effects: 1) the "frozen flow" drift of the entire refractivity distribution due to the prevailing wind (Taylor's hypothesis [25]), combined with 2) turbulent advection during this time period. To investigate which of the two is dominant, we shift a copy of the tropospheric delay signal at t_0 to the position that maximizes the correlation with the observed synthetic interferogram between t_0 and (t_0 + 15 min), yielding the frozen flow synthetic interferogram, see Fig. 6(c). The difference between the observed synthetic interferogram and the frozen flow synthetic interferogram, i.e., Fig. 6(a) and (c), could be regarded as the turbulence-only synthetic interferogram, see Fig. 6(b). Comparison of Fig. 6(b) and (c) shows a clear distinction between the frozen-flow and turbulence-only interferograms. This is confirmed by their power spectra in Fig. 6(e), which are used to analyze the energy distribution of the synthetic interferogram [2]. It shows a clear dominance of the frozen-flow component over the turbulence-only component for wavenumbers smaller than 0.7 cycles/km, hence scales larger than 1.4 km. For smaller scales, there is no significant difference between the two components. The power spectra shown in Fig. 6(e) also provide a convenient stochastic expression of the variability of the atmospheric signal delay, suggesting that the "frozen-flow" approximation is a valid approximation within a time period of up to ∼15'. In other words, for time periods up to ∼15', it is possible to simply consider the atmosphere as a fixed/frozen 3-D refractivity distribution, that translates as a whole with the prevailing wind speed and direction.

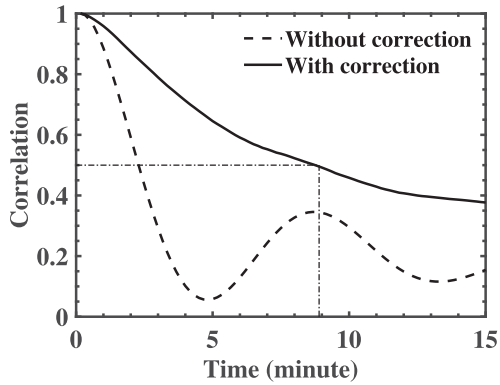

Fig. 7. Correlation coefficient time series relative to the first epoch. Without frozen-flow correction, the signal decorrelates (half-time correlation value) within 3 min. With the correction, this can be lengthened to ∼9 min, see the dot-dashed line.

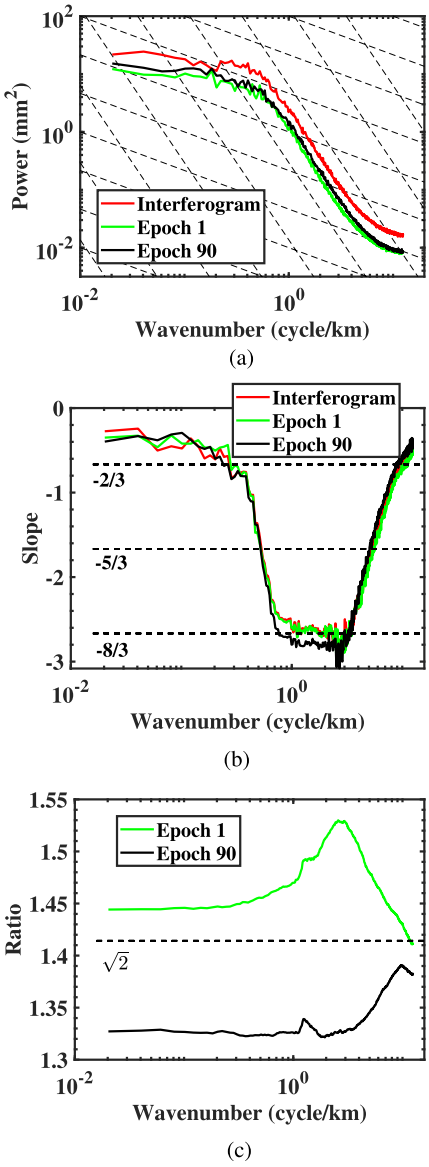

Fig. 8. Comparison of the power spectra between unwrapped 15' synthetic interferogram and the single epoch images. (a) Power spectra. (b) Slope of the power spectra, showing $-8/3$ and $-2/3$ scaling regimes for 0.7–5 km and >8-km ranges, respectively. (c) Ratio of the power spectra between single epoch image and synthetic interferogram. (a) Power spectra. (b) Slope of the power spectra. (c) Ratio of the power spectra.

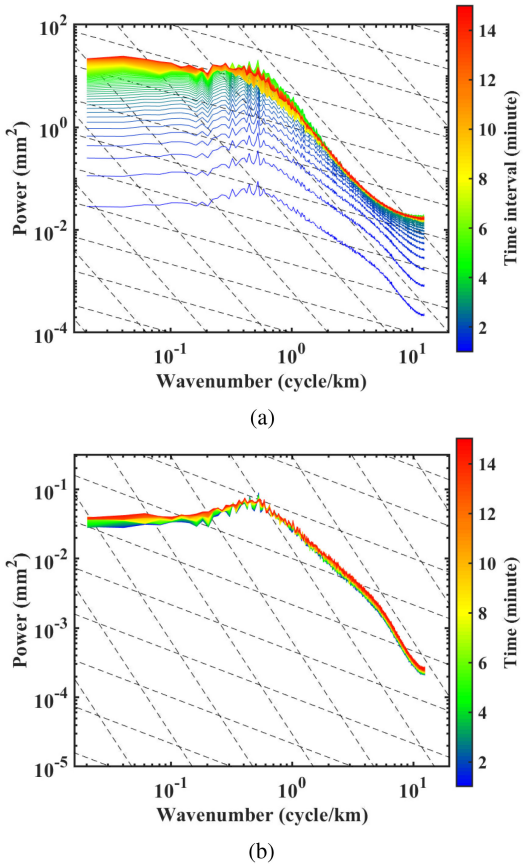

Fig. 9. One-dimensional power spectra synthetic interferogram combinations. (a) Unwrapped single master synthetic interferograms, i.e., cumulatively increasing delays over time. (b) Unwrapped daisy chain synthetic interferograms, i.e., only 10-s time differences. The dashed lines denote $-8/3$ and $-2/3$ power-law behavior. (a) Single master. (b) Daisy chain.

The correlation coefficient time series can be an indicator to express the impact of temporal variations. We compute correlation coefficient time series by comparing the total vertical delay per epoch with the first one, showing the effect of the cumulative total vertical delay, as shown by the dashed line in Fig. 7. This shows that the correlation coefficient drops to less than 0.1 in 5 min, i.e., near-decorrelation. Alternatively, using a correction with the estimated velocity based on Taylor's hypothesis,the corrected correlation coefficient time series are obtained: the solid line in Fig. 7. Compared with the result without velocity correction, the corrected one shows less loss of correlation, suggesting that the decorrelation is dominantly a result of the translation of the entire refractivity distribution as a result of the prevailing wind direction. Yet, after about 9 min the correlation half-time value is reached, which indicates that the use of Taylor's hypothesis is only valid for short time spans.

This result has significant impact for strategies using numerical weather models to correct for atmospheric delay in SAR interferograms. The impact of a temporal, hence spatial, misalignment is very significant, requiring unrealistic temporal alignment constraints on the realization of the model.

Additionally, we compare the tropospheric power spectra between the unwrapped 15' synthetic interferogram and the corresponding single epoch delays, see Fig. 8(a). It shows that the atmospheric delay signals of one epoch and an epoch 15' later are similar in terms of their power and scaling behavior, and that the construction of a synthetic interferogram leads to a differential atmospheric signal that has more power over all of its spatial wavelengths. Fig. 8(b) shows that the scaling behavior is a distinct function of the wavelengths, with the typical $-8/3$ scaling law for scales between 0.7 and 5 km. The less steep power-law slopes for the other wavelengths indicate a more "rough," or noise-like, signal for these domains. The fact that this matches very well suggests that the LES model indeed provides a physically realistic refractivity distribution. As the DALES model is evaluated up to a maximum elevation

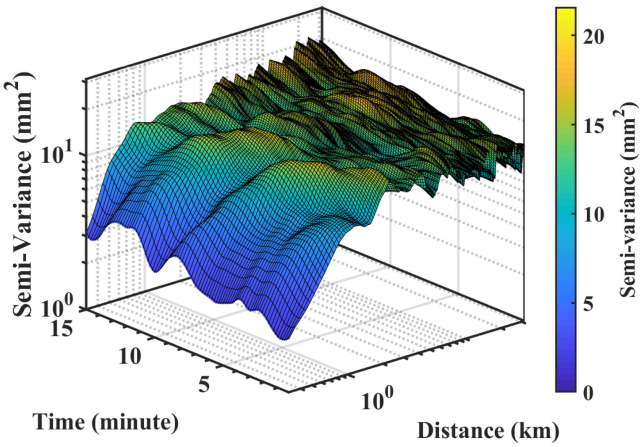

Fig. 10. Spatio-temporal variograms of the total delay for each epoch, showing a sill at a range of ∼1.5 km, and temporal and spatial periodicity.

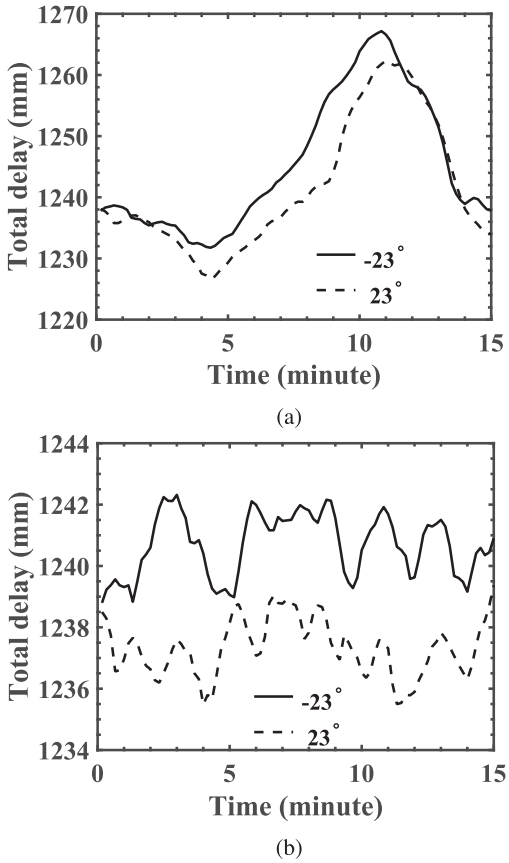

Fig. 11. Total slant delay time series for one pixel for two viewing angles (−23° and 23°, angular difference 46°) for (a) the most changing pixel and (b) the least changing pixel in the domain. Note the differences in range on the vertical axis.

of 4.5 km, the physical interpretation of the results should be limited to horizontal ranges less than ∼5 km, see Fig. 8(b). Fig. 8(c) confirms that the power of the synthetic interferogram is about $\sqrt{2}$ times the power of the atmospheres in single epochs. We note that there is no way to confirm this in real-life situations, since single-epoch signals cannot be obtained unambiguously.

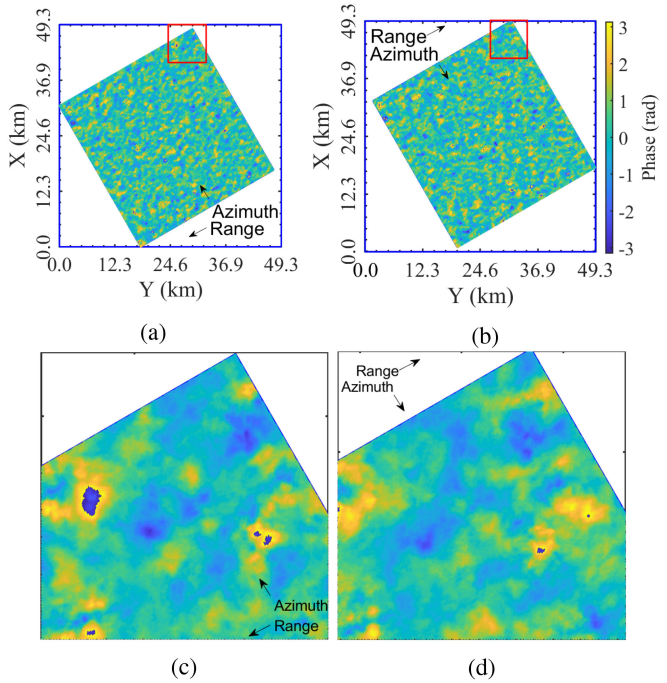

Fig. 12. 15 min tropospheric interferogram (epoch 1–90) with different heading of (a) 300° and (b) 120° and their corresponding magnified views (c) and (d) (Red box in (a) and (b) denotes the test area).

Fig. 9 demonstrates how the power in a synthetic interferogram, for different spatial scales, will increase with increasing temporal separation of the acquisitions. With increasing temporal separation, i.e., the color in Fig. 9(a), we converge to a maximum. For example, at 200-m scales, the colors orange, yellow, and green are obscured by the (longest) 15' temporal separation, while we do see lower power levels for temporal separations up to three minutes. This demonstrates a temporal ceiling of ∼3 min in the energy for scales around 200 m, and of ∼10 min for scales around 10 km. Again, we note that this understanding cannot be obtained from real-life interferograms, as such repeat frequencies are not available for study. Fig. 9(b) demonstrates the amount of power we may encounter in computing so-called "daisy-chain" synthetic interferograms, which have a 10-s separation. These interferograms exhibit a similarly low absolute power, corresponding with very limited spatial variation between subsequent acquisitions, see Fig. 9(b).

Finally, Fig. 10 visualizes the spatio-temporal variograms for each epoch, showing that the semivariance increases as time goes by, a sill at scales of 1500 m, and periodicity in the variance in space and time.

B. Slant Delay Interferogram

Given the satellite orbit parameters, slant delays and (synthetic) interferograms can be obtained using ray-tracing. It is a general analysis for both LEO-SAR and GEO-SAR. Only the viewing (incidence) angle, θ, should be adapted to consider the variety of orbits. In particular, the $(\cos\theta)^{-1}$ ramp is a common term in each single acquisition, which can be neglected since

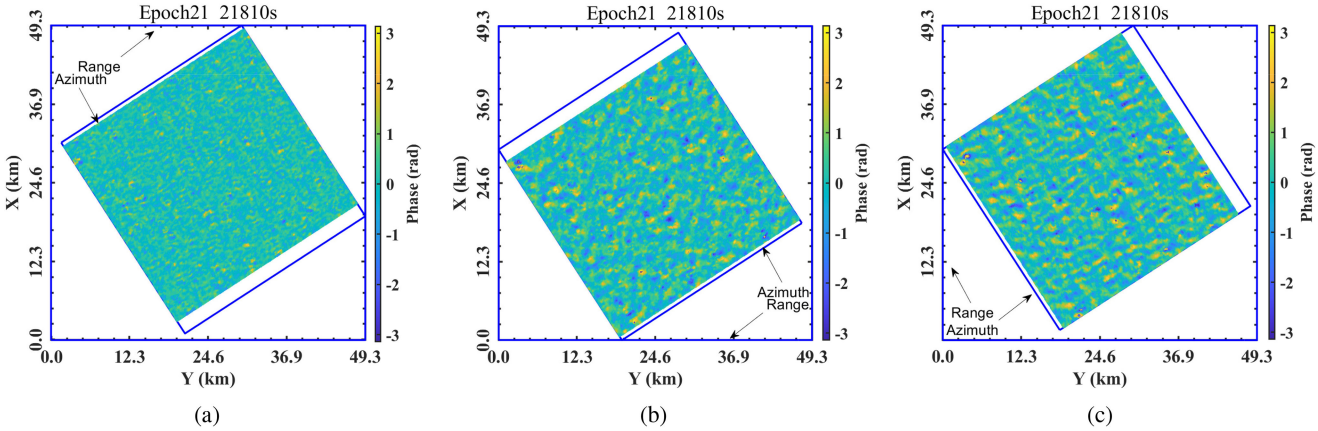

Fig. 13. 210 s tropospheric interferogram (epoch 1–21) with a heading angle of (a) 147°, (b) 327°, and (c) 57°.

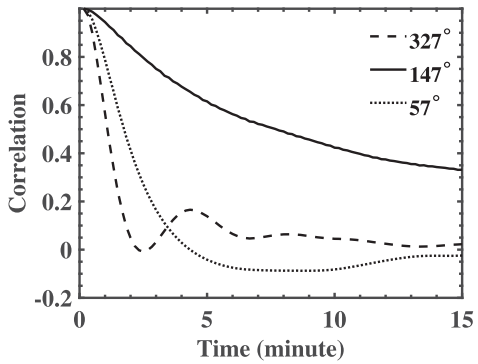

Fig. 14. Correlation coefficient time series relative to the first epoch with different heading angles.

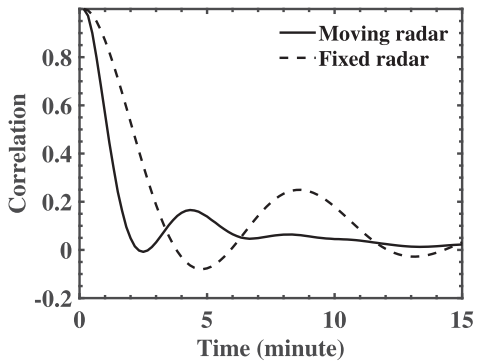

Fig. 15. Correlation coefficient time series relative to the first epoch with an azimuth angles of 327°.

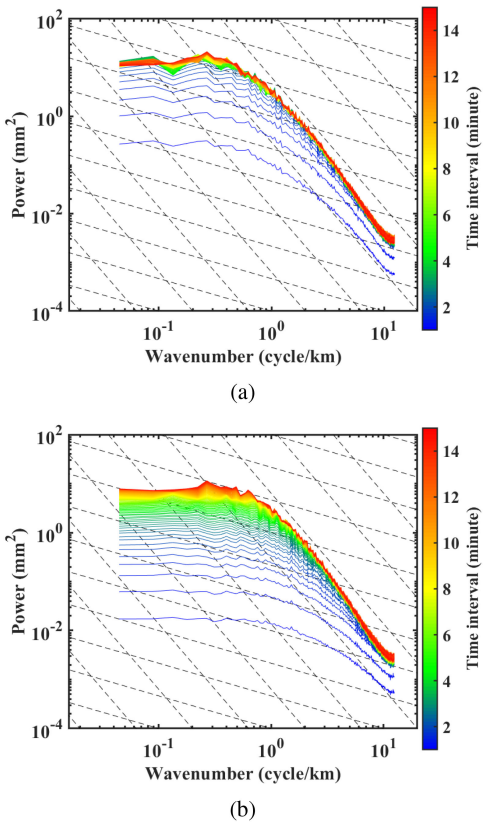

Fig. 16. One-dimensional power spectra combinations of unwrapped single master interferogram with a heading angle of (a) 327° and (b) 147°.

the interferogram is only sensitive to the relative phase change between different acquisitions.

To assess the influence of the temporally changing atmosphere, we show the total slant delay time series of the most and the least changing pixel in the domain, see Fig. 11(a) and (b). During the 15' of the evaluation, the total slant delay varies over ∼40 mm for the most variable pixel (equivalent to 1.4 cycles for C-band), while it varies only within ∼3 mm for the least variable pixel. The latter is negligible during the radar imaging, while the former may have a significant effect in the SAR focusing in case of a GEOSAR imaging geometry.[2]

[2]Obviously, the significantly longer integration times of GEOSAR configurations, in combination with a changing atmospheric refractivity distribution, will influence the focusing, which is not covered in this study. The synthetic interferograms correspond to the APSs (atmospheric phase screens) in asystem with a short integration time and a spatial resolution higher than the troposphere model. This couldn't be applied to short time GeoSAR acquisitions, whose resolution is in the same order of magnitude of the synthetic interferogram spatial variations. In that case, the APS cannot be assumed smooth compared to the system resolution.

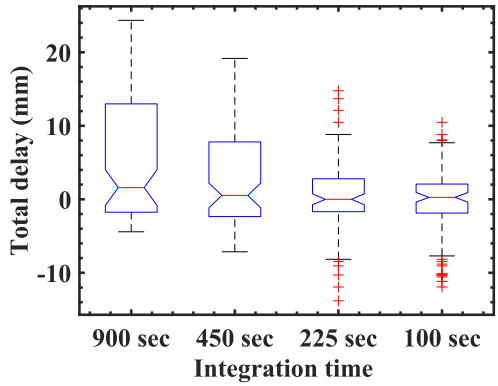

Fig. 17. Variation of the total delay for one location with different integration times.

A change in the viewing geometry during the SAR integration time results in a different path through the atmosphere, and will, therefore, also have an effect on the phase. This may influence the SAR focusing quality, which normally assumes a "frozen" atmosphere during the aperture time [25]. We simulated extreme cases of a difference in viewing angles from $-23°$ to $+23°$, see the solid and dashed lines in Fig. 11(a) and (b). Note that this difference is comparable for LEOSAR satellites with opposing headings (ascending and descending). For these extreme geometric differences, we see that the different path through the atmosphere may lead to more than 10 mm in delay difference over time, for the fair-weather circumstances in this simulation. 15-min tropospheric interferograms with heading angles of 300° and 120°, showing the interferograms of ascending and descending geometry with an angular difference of 46° are shown in Fig. 12(a) and (b). While one would expect to see a mere "shifted" version of the same signal, zoomed-in subsetsshown in Fig. 12(c) and (d) show quite a significant delay difference due to the different viewing geometries. This is due to the complex 3-D distribution of tropospheric refractivity, resulting in different integration paths. Obviously, the viewing geometry differences are extreme for current SAR constellations, but the advent of (combinations of) bistatic and geosnchronous missions will force us to consider such differences.

V. Implications for GeoSAR Orbits

Since the illumination time for GEOSAR is much longer, the space-time variability of the atmosphere may be significant. Variations of the atmospheric state during the SAR illumination time should be considered in the slant delay interferogram, inducing additional space decorrelation. We used the simulated 4-D refractivity distribution to analyze interferograms from a GeoSAR orbit. Table II shows the main parameters of the GeoSAR orbit we used in this simulation. As the time period of the simulation is 15 min, the maximal integration time is 900 s in the following analysis.

A. Analysis of Wind Direction

Based on the analysis of the vertical delay interferogram, the frozen flow plays an important role in the decorrelation of the short term interferograms. Considering the slant delay interferogram, the direction and velocity of the wind with respect to the satelite will directly affect the correlation.

TABLE II
SAR Orbit Parameters

Parameters	values
Semi-major axis [km]	42278.7
Inclination [degrees]	51
Argument of perigee [degrees]	165
Eccentricity	0
wavelength [m]	0.056
incidence (or viewing) angle [degrees]	23
integration time [s]	up to 900

The wind speed of the simulated LES scenario is 3.3 m/s with an azimuth angle of $147°$. Then, setting the velocity of the satellite to this value, the slant delay interferograms with the heading angles of $147°$, $327°$, and $57°$ are obtained. 210-s tropospheric interferograms with heading angles of $147°$, $327°$, and $57°$ are shown in Fig. 13(a)–(c). It shows quite a significant delay difference due to the different viewing geometries. The 210-s tropospheric interferogram with a heading angle of $147°$ has the least spatial variation since the space decorrelation induced by the frozen flow can be neglected, see Fig. 13(a).

The corresponding correlation coefficient time series relative to the first epoch with different heading angles are shown in Fig. 14. It shows that if the wind moves along the same direction as the satellite, the interferometric phase suffers from less decorrelation, which is similar to the result with velocity correlation. In contrast, if the wind direction is opposite to the satellite, it will induce large phase change, i.e., stronger space decorrelation. Fig. 15 shows the correlation coefficient time series with and without space decorrelation, indicating that the space variability leads to faster decorrelation and the correlation coefficient drops to less than 0.1 in two minutes.

Additionally, space decorrelation also changes the one-dimension power spectra of the interferograms with increasing temporal separation, which are shown in Fig. 16. It shows that the lower power levels of the $327°$ interferograms for temporal separations is up to two minutes while that of the $147°$ interferogram is 10 min.

B. Interferograms With Varying Spatial Resolution

During GEOSAR radar imaging, the tropospheric delay may lead to decorrelation in case of long integration times required for high-resolution imaging. To investigate the effect as a function of the spatial resolution, the total delay boxplots with different integration times are shown in Fig. 17, indicating that the variation of the total slant delay during the original integration time (900 s) exceeds 30 mm. If the integration time is limited to 100 s, the change in the total delay ranges from -10 to 10 mm, which is smaller than one cycle. Thus, interferograms with shorter integration times will suffer less from tropospheric delay. Note that the total delays in Fig. 17 are not zero mean since the actual delay is known. In GEOSAR radar imaging, high resolution requires a long integration time, suffering more from the troposphere dynamics, while it has a less influence

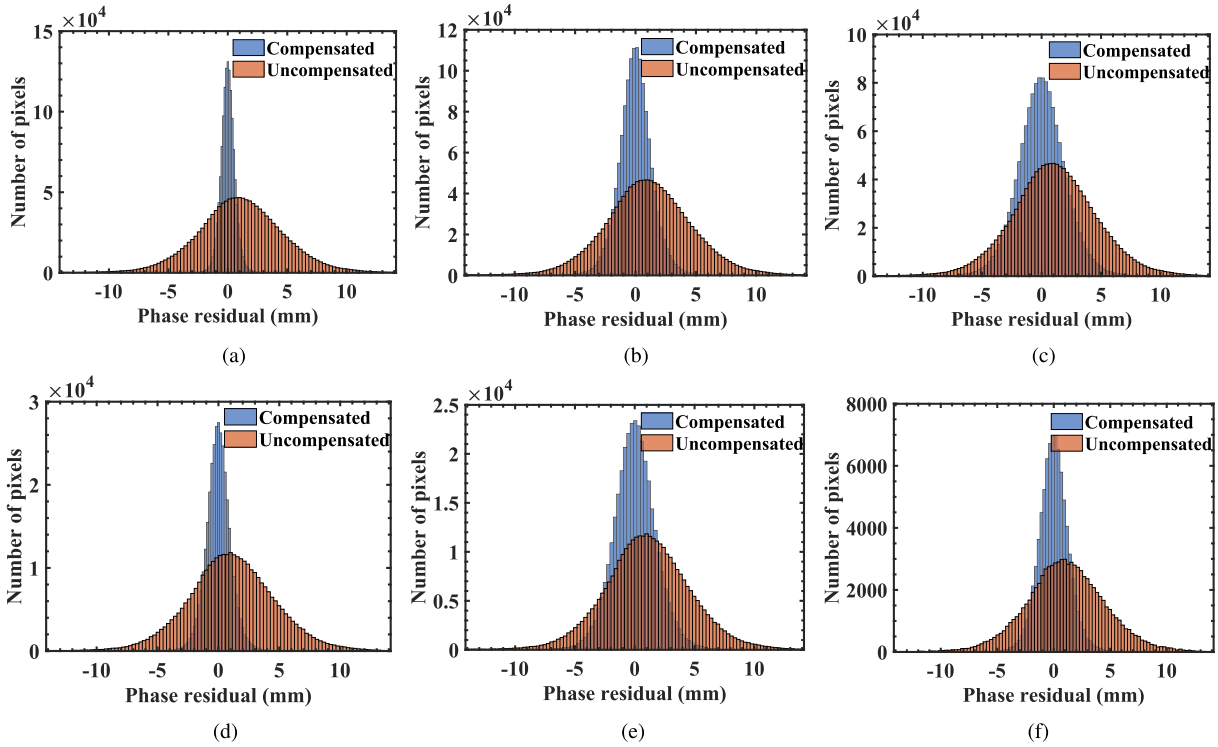

Fig. 18. Effect of integrated refractivity resolution on the phase residual of the compensated interferogram (15 minute single master interferogram). (a)–(c) are compensated 30-m interferograms by 60, 120, and 250-m integrated refractivity. (d) and (e) are compensated 60 m interferograms by 120 and 250-m integrated refractivity. (f) is compensated 120-m interferograms by 250-m integrated refractivity. (a) 30–60 m. (b) 30–120 m. (c) 30–250 m. (d) 60–120 m. (e) 60–250 m. (f) 120–250 m.

on lower resolution images due to the shorter integration time. As a result, the refractivity distribution can be estimated in first order from a low resolution image, which is subsequently used for atmospheric correction of the high resolution image. Based on interferograms with the four resolutions (900, 450, 225, and 100 s there are six potential combinations for multiscale atmospheric correction of the 15' single master interferogram.

Supposing that there are u low-resolution interferograms during the integration time of the high-resolution interferogram. The atmospheric correction part can be expressed using the sum of these low-resolution interferograms, as follows:

$$\phi_L = \sum_{i=1}^{u} e^{-j\phi_L^i}. \tag{13}$$

Then the ϕ_L will be unwrapped, interpolated to the same grid as the high-resolution interferogram and rewrapped. Finally, the rewrapped phase can be used to correct the atmospheric delay in the high-resolution interferogram.

The effectiveness of the atmospheric correction can be evaluated using the phase residuals of the 15' compensated interferogram, which is shown in Fig. 18. Comparing Fig. 18(a)–(c) shows that the larger the difference is between the original and the corrected interferogram resolution, the higher phase SD we get. Phase residuals of the 30-m interferogram corrected by the 60-m interferogram are less than 2 mm, while a correction by the 250-m interferogram leads to phase residuals exceeding 5 mm. Thus, the effects of the troposphere dynamics during radar imaging with long integration times can be well eliminated using the integrated refractivity estimated by interferograms with shorter integration times.

The convenience of the 30–60- or the 30–250-m solutions depends on the spatial and temporal resolution of the DTD. 30–60 is more convenient for fine spatial and low temporal scale variations, while the 30–250 configurationis preferable with fast temporal fluctuations.

VI. Conclusion

Using an advanced large eddy simulation model (DALES) for a fair-weather situation with shallow cumulus convection, typical of continental mid-latitudes, we demonstrated the high value of high-resolution LES models for the realistic spatio-temporal evolution of refractivity in relation to InSAR studies. The results quantify to what extent the turbulent part of the atmosphere contributes to the spatio-temporal variation of the tropospheric delay, and show that the stochastic properties of the LES simulations match with results found in real InSAR studies. We find that the 2-D tropospheric delay signal changes rapidly in time, decorrelating to a half-time value within 3 min. By applying a frozen-flow correction, using the main wind direction as proxy, we can delay this decorrelation to about 9 min. For longer time intervals turbulent advection becomes the dominant part of the signal.

For a particular location in the image, the maximum delay variation can be more than 30 mm within 15 min. Thus, a

temporal misalignment with even a perfect numerical weather model realization may lead to significant interpretation errors in the interferometric phase, for example in deformation studies. This suggests an intrinsic limitation in the ability of weather models to correct InSAR products for tropospheric turbulent delay signals. For future bistatic or GEO SAR missions, with more extreme variability in the viewing geometries and/or longer integration times, our results show that the LES models are effective to quantify the impact of tropospheric delay variability in the design phase.

While the proposed methodology and metrics is demonstrated for a fair-weather situation, it can be easily repeated for cases with more significant turbulence conditions. A DALES-InSAR toolbox is developed to simulate atmospheric phase screens fromthe parameters of DALES and to generate both vertical and slant delay interferograms with specific orbital and viewing parameters, available via GitHub.[3]

ACKNOWLEDGMENT

The authors would like to thank S. Hobbs from Cranfield University and A. Monti-Guarnieri from Politecnico di Milano for support and valuable suggestions. DALES is open-source software, available under the terms of the GNU GPL version 3 at.[4] The DALES-InSAR codes are available at.[5]

REFERENCES

[1] R. Bamler and P. Hartl, "Synthetic aperture radar interferometry," *Inverse Problems*, vol. 14, pp. R1–R54, 1998. [Online]. Available: http://doris.tudelft.nl/Literature/bamler98.pdf

[2] R. F. Hanssen, *Radar Interferometry: Data Interpretation and Error Analysis*. Dordrecht: Kluwer Academic Publishers, 2001.

[3] T. Kobayashi, Y. Morishita, and H. Yarai, "Detailed crustal deformation and fault rupture of the 2015 Gorkha earthquake, Nepal, revealed from scansar-based interferograms of ALOS-2," *Earth, Planets Space*, vol. 67, no. 1, 2015, Art. no. 201.

[4] A. Hooper, P. Segall, and H. Zebker, "Persistent scatterer interferometric synthetic aperture radar for crustal deformation analysis, with application to Volcán Alcedo, Galápagos," *J. Geophysical Res.: Solid Earth*, vol. 112, no. B7, pp. 1–21, 2007.

[5] B. Zhang, R. Wang, Y. Deng, P. Ma, H. Lin, and J. Wang, "Mapping the yellow river delta land subsidence with multitemporal sar interferometry by exploiting both persistent and distributed scatterers," *ISPRS J. Photogrammetry Remote Sens.*, vol. 148, pp. 157–173, 2019.

[6] R. F. Hanssen, T. M. Weckwerth, H. A. Zebker, and R. Klees, "High-resolution water vapor mapping from interferometric radar measurements," *Science*, vol. 283, pp. 1295–1297, Feb. 1999. [Online]. Available: http://doris.tudelft.nl/Literature/hanssen99.pdf

[7] P. Mateus, J. Catalão, G. Nico, and P. Benevides, "Mapping precipitable water vapor time series from sentinel-1 interferometric SAR," *IEEE Trans. Geosci. Remote Sens.*, vol. 58, no. 2, pp. 1373–1379, Feb. 2020.

[8] J. Dorrestijn, D. T. Crommelin, A. P. Siebesma, and H. J. Jonker, "Stochastic parameterization of shallow cumulus convection estimated from high-resolution model data," *Theor. Comput. Fluid Dyn.*, vol. 27, no. 1, pp. 133–148, 2013.

[9] C. Schär et al., "Kilometer-scale climate models: Prospects and challenges," *Bull. Amer. Meteorological Soc.*, vol. 101, no. 5, pp. E567–E587, 2020.

[10] P. Mateus, R. Tomé, G. Nico, and J. Catalão, "Three-dimensional variational assimilation of inSAR PWV using the WRFDA model," *IEEE Trans. Geosci. Remote Sens.*, vol. 54, no. 12, pp. 7323–7330, Dec. 2016.

[11] P. Mateus, P. M. A. Miranda, G. Nico, J. P. S. Catalao, P. Pinto, and R. Tome, "Assimilating InSAR maps of water vapor to improve heavy rainfall forecasts: A case study with two successive storms," *J. Geophysical Res.*, vol. 123, no. 7, pp. 3341–3355, 2018.

[12] K. Tomiyasu, "Synthetic aperture radar in geosynchronous orbit," in *Proc. Antennas Propag. Soc. Int. Symp.*, vol. 16, 1978, pp. 42–45.

[13] R. Haagmans et al., "Earth Explorer 10 candidate mission Hydroterra, ESA report for assessment," Eur. Space Agency, Paris, France, 2020.

[14] M. Lagasio et al., "Meteorological osses for new zenith total delay observations: Impact assessment for the Hydroterra geosynchronous satellite on the Oct. 2019 genoa event," *Remote Sens.*, vol. 12, no. 22, 2020, Art. no. 3787.

[15] J. Wallace and P. Hobbs, *Atmosphere Science: An Introductory Survey*. Cambridge, MA, USA: Elsevier, 1997.

[16] R. Hanssen and R. Klees, "Refractivity maps obtained by radar interferometry," in *Proc. UNAVCO Annu. Meeting*, 1998, p. 1.

[17] T. Heus et al., "Formulation of the dutch atmospheric large-eddy simulation (dales) and overview of its applications," *Geoscientific Model Develop.*, vol. 3, no. 2, pp. 415–444, 2010. [Online]. Available: https://gmd.copernicus.org/articles/3/415/2010/

[18] A. K. Betts, "Non-precipitating cumulus convection and its parameterization," *Quart. J. Roy. Meteorological Soc.*, vol. 99, no. 419, pp. 178–196, 1973.

[19] L. Urquhart, F. Geremia-Nievinski, and M. Santos, "Ray-traced slant factors for mitigating the tropospheric delay at the observation level," *J. Geodesy*, vol. 86, pp. 149–160, 2011.

[20] B. Parkinson, P. Axelrad, and P. Enge, *Global Positioning System: Theory and Applications*. Washington, DC, USA: AAIA, 1996.

[21] F. Alshawaf, S. Hinz, M. Mayer, and F. J. Meyer, "Constructing accurate maps of atmospheric water vapor by combining interferometric synthetic aperture radar and GNSS observations," *J. Geophysical Res.*, vol. 120, no. 4, pp. 1391–1403, 2015.

[22] E. Pichelli et al., "InSAR water vapor data assimilation into mesoscale model mm5: Technique and pilot study," *IEEE J. Sel. Topics Appl. Earth Observ. Remote Sens.*, vol. 8, no. 8, pp. 3859–3875, Aug. 2015.

[23] A. R. Brown et al., "Large-eddy simulation of the diurnal cycle of shallow cumulus convection over land," *Quart. J. Roy. Meteorological Soc.*, vol. 128, no. 582, pp. 1075–1093, 2002.

[24] C. J. Hahn and S. Warren, "A gridded climatology of clouds over land (1971–96) and ocean (1954–97) from surface observations worldwide," U.S. Dept. Energy, Oak Ridge, TN, USA, Tech. Rep. ORNL/CDIAC-153 NDP-026E, 2007.

[25] G. I. Taylor, "The spectrum of turbulence," *Proc. Roy. Soc. London. Ser. A-Math. Phys. Sci.*, vol. 164, no. 919, pp. 476–490, 1938.

[3][Online]. Available: https://github.com/dogfisher/DALES_Atmosphere

[4][Online]. Available: https://github.com/dalesteam/dales

[5][Online]. Available: https://github.com/dogfisher/DALES_Atmosphere

Fengming Hu (Member, IEEE) received the B.E. degree and the Ph.D. degrees in surveying and mapping science and technology from Tongji University, Shanghai, China in 2014 and 2020, respectively.

From October 2017 to October 2019, he was a guest Ph.D. student with the Delft University of Technology, Delft, the Netherlands. Since 2020, he has been a Post-doc with the Key Laboratory for Information Science of Electromagnetic Waves (MoE), Fudan University, Shanghai, China. His research interests include deformation monitoring, 3-D model of the infrastructures, urban change detection and dynamic data processing using synthetic aperture radar images.

Kevin C. Helfer received the M.Sc. degree, in 2016, from Münster University, Münster, Germany, where he did research on double-diffusive convection using finite-volume numerical models, and the Ph.D. degree from the Delft University of Technology, Delft, The Netherlands, in 2021.

He is currently an Atmospheric Scientist with a background in geophysics. He then joined Delft University of Technology, Delft, the Netherlands, to investigate shallow cumulus convection and its interaction with the trade winds, making use of large-eddy simulation. Since then, he has been working for Infoplaza, a Dutch weather company, where he develops innovative weather products, and solutions for consumers and businesses.

A. Pier Siebesma is a Professor of Atmospheric science with the Delft University of Technology, Delft, the Netherlands, and is also affiliated with the Royal Netherlands Meteorological Institute, De Bilt, Netherlands, where he has been researching the role of clouds and convection in our climate system since, 1990. He pioneered the use of Large Eddy Simulations to design parameterisations for cumulus convection that can be used in numerical weather and climate models. During a consultancy with the European Centre of Medium Range Weather Forecasts, he codesigned the Eddy-Diffusivity Mass-flux approach, to parameterize convective transport by cumulus convection in numerical weather prediction and climate models. He has been the coordinator of the FP7 European Project Euclipse (European Union Cloud Intercomparison, Process Study and Evaluation Project).

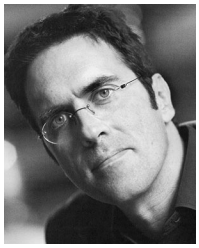

Ramon F. Hanssen (Senior Member, IEEE) received the M.Sc. degree in geodetic engineering and the Ph.D. degree (cum laude) from the Delft University of Technology, Delft, The Netherlands, in 1993 and 2001, respectively.

He was with the International Institute for Aerospace Survey and Earth Science, Stuttgart University, Stuttgart, Germany; the German Aerospace Center (DLR), Weßling, Germany; Stanford University, Stanford, CA, USA, as a Fulbright Fellow; and the Scripps Institution of Oceanography, University of California at San Diego, La Jolla, CA, USA, involved in microwave remote sensing, radar interferometry, signal processing, and geophysical application development. Since 2008, he has been an Antoni van Leeuwenhoek Professor of Earth Observation with the Delft University of Technology, where he has been leading the research group on mathematical geodesy and positioning, since 2009. He has authored a textbook on radar interferometry.